

# Testing Enlil’s Ability to Predict CIR Three Dimensional Structure

T.W. Broiles  
Southwest Research Institute

May 1, 2014

## Abstract

The radial alignment of ACE and Ulysses in February 2004 and August 2007 provided us with unprecedented opportunities to study the radial evolution of planar magnetic structures in 3 corotating interaction regions (CIRs). The in-situ observations are compared with results from a numerical model of CIRs [Odstreil, 2003]. We find that: 1) All 3 CIRs’ meridional tilt retained its North/South orientation at ACE and Ulysses, but the evolution was not systematic. Further, the model results of CIR meridional tilt do not agree with observations. 2) All 3 CIRs rotated azimuthally with the Parker spiral as expected, however model results only describe this behavior quantitatively for 1 CIR. We suggest that the evolution of meridional tilt from ACE to Ulysses did not agree with projections because the parent coronal holes were highly structured. We also suggest that observations of azimuthal tilt do not agree with the model results because the models may underestimate transverse flows, whereas in reality, these flows could affect the observed azimuthal tilt of the CIR. The local orientation of PMSs within CIRs may also be distorted by transients, but their effect is unclear.

## 1 Introduction

Corotating Interaction Regions (CIRs) are compression regions that form along the boundary between slow and fast solar wind. CIR shape is a consequence of radial solar wind flow, solar rotation, and the local topography of the solar wind source regions in the corona (i.e., coronal hole and streamer belt shape) [Pizzo, 1991; Lee, 2000]. Thus, the CIR is also expected to rotate azimuthally like the spiral structure of the interplanetary magnetic field (IMF) as it moves out in the heliosphere [Pizzo, 1991; Lee, 2000]. Further, the shape of the parent coronal hole determines the CIRs meridional tilt, which becomes more perpendicular to the ecliptic plane as it moves away from the Sun [Pizzo, 1991; Lee, 2000].

The boundary between the slow and fast solar wind is known as the stream interface, and is a tangential discontinuity that forms near the Sun because of flow shear between the two streams [Pizzo, 1991]. A tangential discontinuity is impermeable to the interplanetary magnetic field (IMF) and the surrounding solar wind [Belcher and Davis, 1971]. The inability of plasma to move across this boundary causes pressure waves to form on either side of the CIR. In the CIR reference frame, solar wind approaches from either side and introduces surrounding IMF into the compression region [Clack *et al.*, 2000]. The newly compressed IMF will be flattened into a planar magnetic structure (PMS), which has been found to be aligned with the CIR as a whole [Clack *et al.*, 2000].

Observations of CIR topology have been made at both ACE and Ulysses [Clack *et al.* [2000, and references therein]. Recently, Broiles *et al.* [2012] identified 153 CIRs at ACE and studied the properties of PMSs for 74 events.

Study of CIR properties using three-dimensional magnetohydrodynamic (MHD) models has improved dramatically over the last decade. Odstreil [2003] developed Enlil, which predicts the solar wind velocity, proton density, proton temperature, and magnetic field vectors. The events are simulated using a coupled

solar corona/solar wind model. In particular, we use the Wang-Sheeley-Argé method (WSA) or the MHD Algorithm Around a Sphere (MAS) to calculate the outer coronal boundary conditions [Wang and Sheeley, 1990; Argé and Pizzo, 2000; Lionello *et al.*, 2003]. The coronal solution is provided to the Enlil solar wind model, which calculates the global solar wind conditions from the outer boundary of the coronal model to 10 AU. Lee *et al.* [2009] made a statistical comparison of the model's results to the plasma and magnetic field parameters during the declining phase of solar cycle 23. Jian *et al.* [2011] compared results from WSA-Enlil and MAS-Enlil with observations of the bulk plasma and magnetic field in CIRs at ACE and Ulysses during their latitudinal alignment in 2004. Both studies found that Enlil was capable of capturing the large-scale structure and bulk plasma properties of CIRs in the solar wind, but had trouble predicting the fine structure, arrival times, and compression strength.

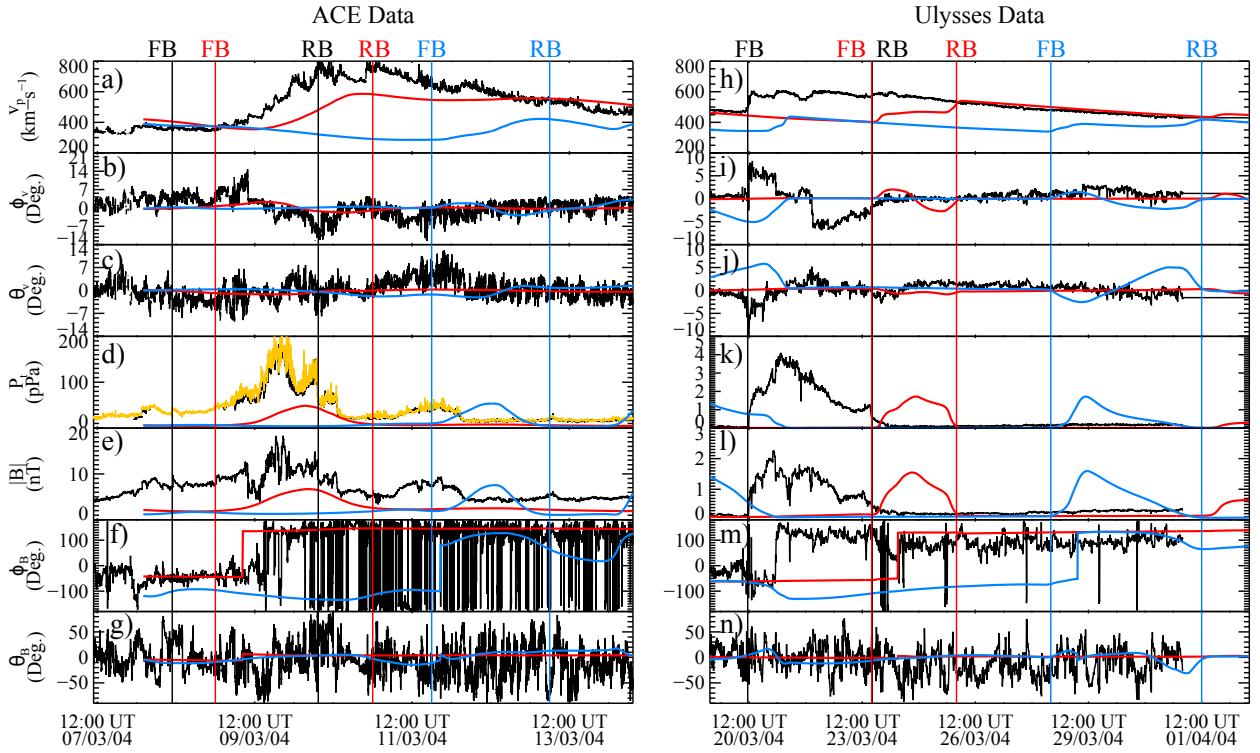


Figure 1: CIR 2 observed at both ACE (left panels) and Ulysses (right panels) (CIR 2 in Table 1). Top to bottom, (a, g) solar wind speed ( $\text{km s}^{-1}$ ), (b, h) total pressure (pPa), (c, i) magnetic field strength (nT), (d, j) R magnetic field component (nT), (e, k) T magnetic field component (nT), and (f, l) N magnetic field component (nT). Black data: observations. Red data: WSA-Enlil. Blue data: MAS-Enlil. Vertical black lines: forward boundary (FB) and reverse boundary (RB) of the observed CIR. Vertical red lines: forward boundary (FB) and reverse boundary (RB) of the WSA-Enlil CIR. Vertical blue lines: forward boundary (FB) and reverse boundary (RB) of the MAS-Enlil CIR. Gold data in panel b is time-shifted Wind data to the position of ACE, which is used to fill data gaps.

In this paper we highlight some of the work of Broiles *et al.* [2013], which studied Enlil's ability to predict the orientation of CIRs. In this work, we will discuss how they compared observations of planar magnetic structures in 3 CIRs at ACE and Ulysses when the two spacecraft were near radial alignment, then compared those observations with Enlil results of the global CIR shape [Odstrcil, 2003]. For brevity, we will only discuss the results of CIR 2 from the work of Broiles *et al.* [2013], but these results were typical of the entire study.

## 2 Observations of CIR Properties at ACE and Ulysses

### 2.1 Evolution of Bulk CIR Properties

We use the Solar Wind Electron, Proton, and Alpha Monitor (SWEPAM) [McComas *et al.*, 1998] and the Magnetometer (MAG) [Smith *et al.*, 1998] instruments onboard the Advanced Composition Explorer (ACE) [Stone *et al.*, 1998], and the Solar Wind Observations Over the Poles of the Sun (SWOOPS) [Bame *et al.*, 1992] and the Magnetometer (FGM) [Balogh *et al.*, 1992] instruments onboard Ulysses [Wenzel *et al.*, 1992]. SWOOPS and SWEPAM measure the energy/charge distribution of solar wind ions every minute, which is used to derive key solar wind parameters such as density, bulk speed, and temperatures for both protons and alphas. We use 1 minute magnetometer data to provide the magnetic field vector.

From a list of 153 CIRs studied by Broiles *et al.* [2012] at ACE and Wind [Acuña *et al.*, 1995], we identify 3 that were also observed at Ulysses when the Earth-Sun-Ulysses angle was less than  $24^\circ$ . Table 1 lists the details of the 3 CIRs, and will be discussed in § 2.2. CIRs 1 and 2 were observed at ACE on 11 Feb. and 8 Mar. 2004, and later at Ulysses near 5 AU. CIR 3 was observed at ACE on 26 Aug. 2007, and at Ulysses at a radial distance of  $\sim 1.4$  AU. We estimated the arrival time for each CIR at Ulysses by adding solar rotation time between the spacecraft (i.e., the longitudinal difference between spacecraft,  $\Delta\phi$ , divided by the solar rotation rate) and the radial propagation time (i.e., the radial distance between spacecraft divided by the mean solar wind speed of the CIR measured by ACE). CIRs 1 and 2 took nearly 15 days to travel  $\sim 4$  AU from ACE to Ulysses, while CIR 3 took 2.2 days because the spacecraft were separated by only  $\sim 0.4$  AU during the fast latitude scan of Ulysses.

Figure 1 shows solar wind and magnetic field properties (black) associated with CIR 1 at ACE (left panels) and Ulysses (right panels). Additionally, it includes WSA-Enlil (red) and MAS-Enlil (blue) simulations of these quantities at each spacecraft. The data from WSA-Enlil and MAS-Enlil has been shifted in time such that the predicted and observed CIR's stream interface occur at the same time. We discuss these model results in detail in § 3. From top to bottom, the figure shows: (a, h) solar wind speed, (b, i) solar wind azimuthal deflection angle, (c, j) solar wind meridional deflection angle, (d, k) total pressure, (e, l) magnetic field strength, (f, m) azimuthal, and (g, n) meridional magnetic field angles. All angles are in the Radial-Tangential-Normal (RTN) coordinate system [Fränz and Harper, 2002].

At ACE, the forward boundary is identified by the small increase in total pressure (Fig. 1d) and magnetic field strength (Fig. 1e). The stream interface is observed to have an increase in solar wind speed (Fig. 1a), an increase in proton temperature (not shown), a increase in proton temperature (not shown), and a transition from positive to negative in the azimuthal solar wind deflection angle (Fig. 1b). The reverse boundary is identified by an increase in solar wind speed (Fig. 1a), a decrease in total pressure (Fig. 1d), and a decrease in magnetic field strength (Fig. 1e). Approximately 12.5 days later, CIR 2 was observed at Ulysses; the forward boundary is identified by the abrupt increases in solar wind speed (Fig. 1h), total pressure (Fig. 1k), and magnetic field strength (Fig. 1l). The stream interface had similar plasma properties to those observed at ACE. The reverse boundary is identified by an increase in solar wind speed (Fig. 1h) and a decrease

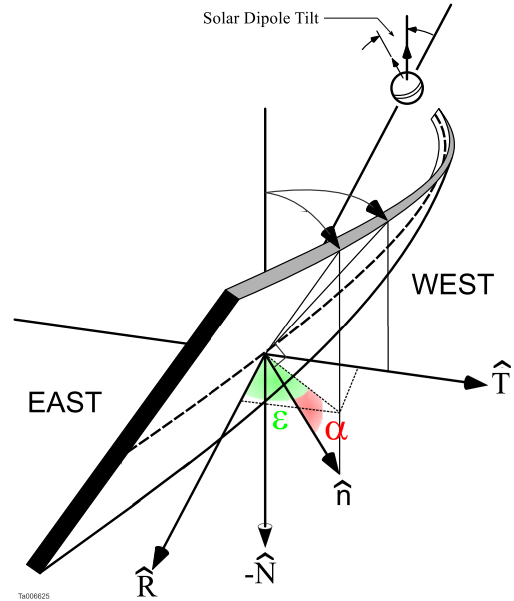


Figure 2: A schematic CIR that shows the CIR wave front, its normal vector,  $\hat{n}$ , the RTN coordinate system, and the angles  $\alpha$  (red) and  $\epsilon$  (green). Modified from Pizzo [1991].

in total pressure (Fig. 1k). The IMF polarity rotated from outward to inward ahead of the SI (Figures 1f and 1m), again indicating the crossing of an HCS. This CIR was also identified at Ulysses in the above mentioned list. We also note that the proton temperature and plasma  $\beta$  were anomalously low ahead of the forward boundary of CIR 2 at ACE (not shown), which may indicate the presence of an ICME [Zurbuchen and Richardson, 2006].

## 2.2 Evolution of Planar Magnetic Structures

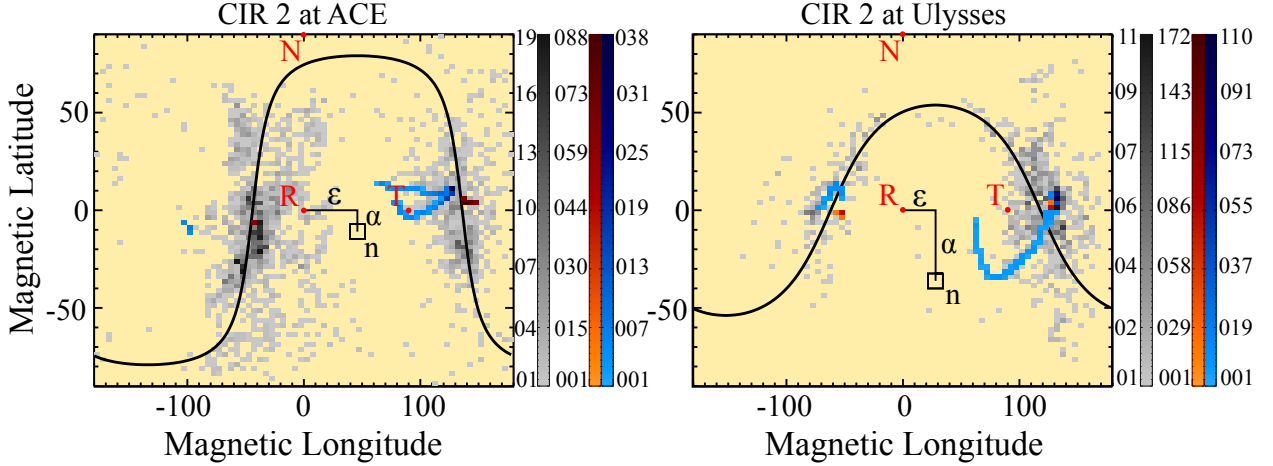


Figure 3: Two-dimensional histograms of magnetic field latitude vs. longitude for CIR 2 at ACE (left) and Ulysses (right). Gray-scale pixels: Observed magnetic field, Red-scale pixels: WSA-Enlil magnetic field, and Blue-scale pixels: MAS-Enlil. Red dots: RTN axis, black square: normal vector to PMS, and black curves connecting the radial unit vector to the normal vector: the angles  $\alpha$  and  $\epsilon$ . Black wave-like curve: the plane determined through MVA.

Table 1 shows the times of the forward boundary, stream interface, and reverse boundary of each CIR, observation latitude,  $\theta$ , heliographic longitude of Ulysses relative to the Earth,  $\Delta\phi$ , and the orientation of the PMSs for all 3 CIRs at both ACE (unshaded) and Ulysses (shaded). The orientation of the PMSs are calculated using Minimum Variance Analysis (MVA) [Sonnerup and Cahill, 1967], which uses the covariance matrix of a set of three dimensional vectors (i.e., all the magnetic field vectors measured between the forward and reverse boundaries of a CIR) to calculate the direction of minimum variance. The direction of minimum variance is the normal vector,  $\hat{n}$ , that defines the PMS [Sonnerup and Cahill, 1967]. We note that MVA cannot determine higher-order curvature in the magnetic structure without using observations from multiple spacecraft [Paschmann and Daly, 1998]. We transform the normal vector into a spherical coordinate system, with an azimuthal angle,  $\epsilon$ , and a meridional angle,  $\alpha$  (i.e.,  $\alpha = \arcsin(n_N/|\hat{n}|)$ ,  $\epsilon = \arctan(n_T/n_R)$ ). The angles  $\alpha$  (red) and  $\epsilon$  (green) are shown in the schematic of a CIR in Figure 2.

In addition to verifying by eye that each event can be reasonably represented as a PMS, we also required that the uncertainties in  $\alpha$  and  $\epsilon$  were less than  $5^\circ$  [Khrabrov and Sonnerup, 1998], the ratio of intermediate to minimum variance was greater than or equal to 2.5, and the average ratio of the magnetic field component normal to the PMS over the magnetic field strength was less than or equal to 0.2 (i.e.,  $\Delta\alpha$  and  $\Delta\epsilon < 5^\circ$ ,  $\lambda_{Int.}/\lambda_{Min.} \geq 2.5$ , and  $\langle B_N/|B| \rangle \leq 0.2$ ). These criteria are typically used in the literature for identifying PMSs [Neugebauer et al., 1993; Paschmann and Daly, 1998; Clack et al., 2000].

Figure 3 shows a two-dimensional histogram of magnetic field vectors between the forward and reverse boundaries of CIR 2 at ACE (left) and Ulysses (right) in latitude vs. longitude. Figure 3 also includes magnetic field vectors from WSA-Enlil (red) and MAS-Enlil (blue) models, which are discussed in § 3. From

#	FB	RB	$\theta$ (°)	$\Delta\phi$ (°)	$\alpha$ (°)	$\epsilon$ (°)	$\langle \mathbf{B}_N /  \mathbf{B}  \rangle$	$\lambda_{Int.} / \lambda_{Min.}$
1	09:19 11/2/04	10:33 12/2/04	-6.67	15.33	$20.7 \pm 0.7$	$45.1 \pm 0.5$	0.09	6.7
	04:02 25/2/04	22:47 28/2/04	-0.23	1.23	$19.1 \pm 0.4$	$8.4 \pm 0.1$	0.04	5.9
2	10:50 8/3/04	07:23 10/3/04	-7.24	-10.79	$-10.9 \pm 1.0$	$46.0 \pm 0.4$	0.07	3.0
	11:05 20/3/04	18:21 23/3/04	-1.42	-22.74	$-34.4 \pm 0.8$	$27.9 \pm 0.3$	0.06	2.7
3	08:31 26/8/07	00:47 27/8/07	7.05	6.75	$33.4 \pm 0.8$	$24.4 \pm 0.6$	0.10	7.8
	09:29 28/8/07	07:52 29/8/07	14.04	5.09	$18.8 \pm 1.0$	$13.5 \pm 0.6$	0.01	4.2

Table 1: Dates and times of the forward boundaries (FB), stream interfaces (SI), and reverse boundaries (RB) for all three CIRs studied at ACE and Ulysses (gray shading), column 3: the observing spacecraft’s heliographic latitude,  $\theta$ , column 4: the difference in heliographic longitude between ACE and Ulysses,  $\Delta\phi$ , column 5:  $\alpha$ , column 6:  $\epsilon$ , column 7:  $\langle \mathbf{B}_N / |\mathbf{B}| \rangle$ , and column 8:  $\lambda_{Int.} / \lambda_{Min.}$ .

Table 1 and Figure 3, the azimuthal angle  $\epsilon$  is noticeably smaller for all three CIRs at Ulysses, suggesting that the CIRs rotated en route from ACE to remain aligned with the Parker spiral. However,  $\alpha$  behaved differently for each CIR between ACE and Ulysses; for CIR 1 there was no change, for CIR 2 the magnitude of  $\alpha$  increased, and for CIR 3 the magnitude of  $\alpha$  decreased. We note that for CIR 1, the MVA-determined meridional tilt is northern, while the meridional deflection angle transitioned from negative to positive within the event observed at Ulysses (Fig. 1j), suggesting a southern tilt [Pizzo, 1991; Lee, 2000].

### 2.3 Observations of the Associated Coronal Holes

Gosling *et al.* [1993] studied the deflection of solar wind by CIRs observed at high latitudes by Ulysses, and found that CIRs typically deflected the solar wind equatorward ahead of the stream interface and poleward behind it. This deflection of solar wind suggests that coronal holes in the northern hemisphere produce CIRs with southern tilt and coronal holes in the southern hemisphere produce CIRs with northern tilt. Based on the heliographic latitudes of the spacecraft shown in Table 1 and the observed relationship between PMS meridional tilt and meridional solar wind deflection angles [Broiles *et al.*, 2012], we expect that CIRs 1, 2, and 3 would respectively have northern, northern, and southern tilts, at ACE and Ulysses. However, the expected meridional tilts only agree with observations in the case of CIR 1. Therefore, we perform a more detailed study of the coronal holes associated with the CIRs in this study.

Figures 4 a, b, and c respectively show SOHO EIT 195 Å images of the corona at the time when the high speed streams that caused CIRs 1, 2, and 3 were expected to leave the Sun. The time that each image was taken is included in the bottom left of each panel. Eq. 1 estimates the longitude,  $\phi_0$ , where the solar wind left the source surface,  $r_0$ , using the spacecraft heliocentric distance,  $r$ , the spacecraft longitude relative to the Earth,  $\phi$ , the solar rotation rate,  $\Omega$ , the average solar wind speed,  $\langle V \rangle$ , and when the spacecraft observed the solar wind,  $t_{Obs.}$ . The latitude of each spacecraft, projected onto the source surface, is also shown in each image. However, we note that the solar wind may not necessarily originate from the same latitude because the near-Sun solar wind may have non-radial flows [Neugebauer *et al.*, 1998]. Red lines connect the origin of the predicted solar wind associated with the forward and reverse boundaries of the CIR, as observed at each spacecraft

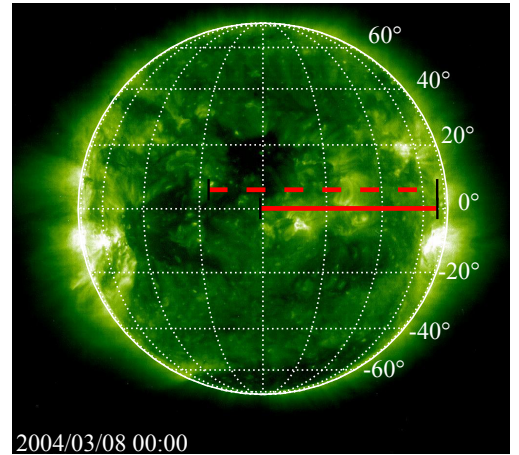


Figure 4: SOHO EIT 195 Å images of the corona when CIR 2 were calculated to leave the Sun. Solid and dashed lines: where the solar wind, associated with the CIR at ACE and Ulysses, originated from.

(i.e., Ulysses: dashed lines, ACE: solid lines).

$$\phi_0 = \phi - \left( t_{Obs.} - \frac{r - r_0}{\langle V \rangle} \right) \Omega, \quad \phi = \begin{cases} 0, & \text{ACE.} \\ -\Delta\phi, & \text{Ulysses.} \end{cases} \quad (1)$$

Figure 4 shows several important features about the origins of the CIRs in this study: (1) The coronal hole associated with CIR 2 appear to be the dark region near the center of the disk in each image. (2) The associated coronal hole has a complex shape, which cannot be approximated as circular. (3) The coronal hole associated with CIR 2 lays to the west of active regions, which could produce the transients observed ahead of CIR 2 (see Figure 1).

### 3 Comparison with Enlil Model Results

#### 3.1 Predictions of the Bulk Plasma and Magnetic Field Properties

We now compare our observations with with three-dimensional MHD simulation results. While many models have been developed, we chose to compare our observations with results from WSA-Enlil and MAS-Enlil [Odstreil, 2003] for several reasons: 1) the models are available for runs-on-request at the Community Coordinated Modeling Center (CCMC), 2) the coronal models, MAS and WSA, use full Carrington rotation synoptic maps of the photosphere to generate numerical solar wind results, and 3) the output numerical results include in-situ vectors of the IMF at ACE and Ulysses, which we can directly compare with the observed magnetic field vectors. At the CCMC, synoptic photospheric maps from the National Solar Observatory (NSO), Mount Wilson Observatory (MWO), or from the GONG Observatory are available as input into the MAS and WSA coronal models. Each observatory uses different calibration techniques to create the publicly available maps, and consequently, the coronal results from WSA and MAS will vary depending on the input maps used [Neugebauer *et al.*, 1998; Arge and Pizzo, 2000; Arge *et al.*, 2004; Lee *et al.*, 2009]. Jian *et al.* [2011] found that WSA-Enlil best predicted fast solar wind speeds and CIR arrival times when NSO synoptic maps were used. Additionally, NSO synoptic maps were the only option available for all 3 Carrington rotations studied. Therefore, we used NSO synoptic maps as input for WSA and MAS.

All the simulations were requested with version 2.7 of Enlil at the highest resolution available. For CIRs 1 and 2, the models had a grid of 1280x45x180 cells with a spatial resolution  $1.7 R_{Sun} \times 2^\circ \times 2^\circ$ . Ulysses was near 1.4 AU during CIR 3, which allowed us to reduce the outer boundary of Enlil to 2 AU and use a finer grid of 1024x120x360 with a spatial resolution of  $0.41 R_{Sun} \times 1^\circ \times 1^\circ$ . The CCMC includes magnetograms up to 60 days before the start of the requested Carrington rotation in order to account for the ambient solar wind that left the Sun prior to that time.

In order to compare the model's results with our observations, we performed a coordinate transformation of the model's magnetic field results from the Enlil Heliospheric Numerical Model (HNM) to HGRTN coordinates [Fränz and Harper, 2002]. The coordinate transform is calculated as follows: 1) A rotation about the z-axis by  $180^\circ +$  the longitudinal separation of the spacecraft from the Earth,  $\Delta\phi$ . 2) A rotation about the y-axis by the heliographic latitude of the spacecraft,  $\theta$  (i.e., the following Euler rotation  $(180^\circ + \Delta\phi, \theta, 0)$ ).

The WSA-Enlil and MAS-Enlil results for each CIR are respectively shown in Figure 1 as red and blue curves. Identically colored vertical lines mark the boundaries of the simulated CIRs. With the exception of WSA-Enlil for CIR 3, the models predict all of the observed CIRs in our study. However, there were timing offsets between the model results and observations for all runs except for WSA-Enlil for CIR 1. Also, both MAS-Enlil and WSA-Enlil underestimate the compression of the magnetic field and total pressure within all three CIRs. We do not discuss these effects further, because they are beyond the scope of this work and



have been discussed previously by *Owens et al.* [2008], *Lee et al.* [2009], *Jian et al.* [2011], and references therein.

### 3.2 Predictions of the CIR Orientation

Figure 5 shows WSA-Enlil results for CIR 2, which includes the predicted radial speed in the T-N plane at the inner boundary of the model (Fig. 5a) along with cross-sections of the total pressure multiplied by heliocentric radius squared (i.e.,  $P*r^2$ ) in the R-T and R-N planes at the latitudes and longitudes of ACE (Fig. 5 b, c) and Ulysses (Fig. 5 d, e). In panels b-d, we show the MVA analysis results of Figure 3 as white arrows with a red outline; perpendicular white lines have been included to make a direct comparison to the compression region produced by the model. These lines do not always appear perpendicular to their arrow counterpart in panels b-e because of the non-uniform aspect ratio of the axes. Dates above panel a show when that longitude was the central meridian to the Earth.

We have repeated the analysis shown in Figure 4 to identify the relevant high-speed stream in Figure 5a and confirm that the predictions (Figure 1 red curves) and observations (Figure 1 black data) have the same origin. We estimate when the solar wind crossed the inner boundary of the Enlil model,  $r_0$  (WSA-Enlil  $21.5 R_{Sun}$ , MAS-Enlil:  $30 R_{Sun}$ ), using Eq. 1 again. Because  $r_0$  is past the sonic point in this version of the analysis, we can assume that the solar wind flow is purely radial, and consequently that the solar wind came from the same heliographic latitude as the spacecraft when it observed the CIR. Black arrows connect the origin of the predicted solar wind associated with the forward and reverse boundaries of CIR 2 for each spacecraft (i.e., Ulysses: dashed arrow, ACE: solid arrow), while vertical tick marks show the same analysis for the observed solar wind.

We note the following: 1) The predicted and observed CIR left the Sun near the same time, and is likely associated with the high-speed stream in the center of Fig. 5a. 2) The azimuthal tilt of the predicted compression region agrees with the PMS at ACE (Fig. 5b), but is more tangential at Ulysses than is observed (Fig. 5d). 3) The meridional tilt of the predicted compression region agrees with the PMS at ACE (Fig. 5c), but is more perpendicular to the solar equatorial plane than the PMS at Ulysses (Fig. 5e).

## 4 Discussion and Conclusions

The near-radial alignment of ACE and Ulysses in February 2004 and August 2007 provided us with unprecedented opportunities to study the evolution of PMSs within 3 individual CIRs. Our results are:

1. The meridional tilt,  $\alpha$ , retained its North/South orientation at ACE and Ulysses, but it does not evolve systematically and could not be predicted by WSA-Enlil or MAS-Enlil.
2. The azimuthal tilt,  $\epsilon$ , systematically rotates towards 0, remaining aligned with the Parker spiral as expected, but WSA-Enlil and MAS-Enlil only predicted its evolution for CIR 1.

Table 2 summarizes the comparisons between our observations and simulations based on WSA-Enlil (red rows) and MAS-Enlil (blue rows). From left to right, columns include: 1) the CIR number, 2) the observing spacecraft, 3) the model that predictions are based on, 4) comparison of  $\epsilon$  to the predicted CIR's azimuthal tilt, 5) comparison of  $\alpha$  to the predicted CIR's meridional tilt, and 6) the location on the Sun where the observed and predicted CIR originated from. Projections of CIR meridional tilt are dependent on observations at ACE, and consequently are excluded from the Table.

### 4.1 Evolution of CIR Meridional Tilt

The evolution of meridional tilt is unique to each CIR;  $\alpha$  does not evolve systematically towards 0 as expected. In CIR 1,  $\alpha$  showed no change between ACE and Ulysses, while in CIRs 2 and 3,  $\alpha$  rotated away

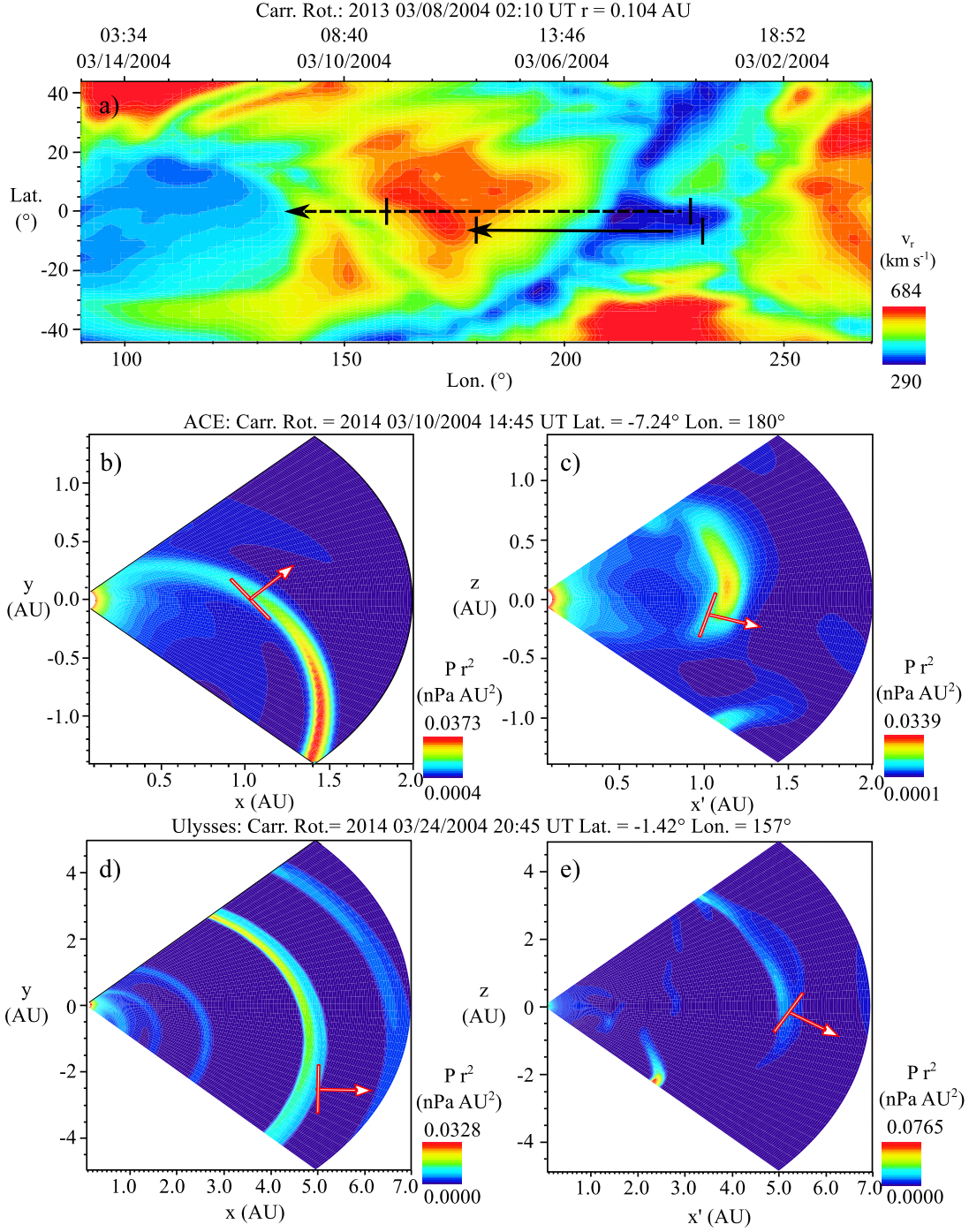


*Figure 5: WSA-Enlil contour plots of CIR 2 showing (a) solar wind radial speed at the model's inner boundary, cross-sections of pressure multiplied by heliocentric distance squared in (b, d) the R-T plane and (c, e) R-N plane at ACE and Ulysses. Solid and dashed arrows: where WSA-Enlil predicted solar wind, associated with CIR 1 at ACE and Ulysses, originated from, vertical tick marks: where the observed solar wind, associated with CIR 1 at ACE and Ulysses, originated from. In panels b-d, white arrows show the relevant spacecraft's position and the results of our MVA analysis on the observations; perpendicular white lines show the orientation of the PMS.*



from and toward the ecliptic, respectively. In contrast to the observations of meridional tilt,  $\alpha$ , analytical projections based on the model of *Lee* [2000] (not shown) predict a systematic decrease with increasing radial distance.

Moreover, the WSA-Enlil and MAS-Enlil simulations were also unable to predict the evolution of  $\alpha$  between spacecraft. Both WSA and MAS use photospheric synoptic maps to predict the solar wind speed, which should account for differences in speeds at the latitudes of each spacecraft. Additionally, the synoptic maps have been smoothed, which may cause the shape of the predicted high-speed stream (Figure 5a) to be over-simplified. Another possibility is that low grid resolution in Enlil, a constraint to make CCMC simulations computationally inexpensive, also causes WSA-Enlil and MAS-Enlil to underestimate CIR fine structure in interplanetary space.

Therefore, we suggest that the disagreement between model results and observations is related to localized differences in the orientation of the parent coronal hole’s leading edge,  $d$ , which we had assumed was the same for the CIR at ACE and Ulysses. Recently, complex coronal hole boundaries have been proposed by *Antiochos et al.* [2011], while *Schwenn* [1990] and *Crooker et al.* [2010] found observational evidence supporting this hypothesis. Thus, if coronal hole boundaries are complex and change within a few degrees of heliolatitude, then it would be unlikely for model results of CIR meridional tilt to agree with observations from a different latitude.

The notion that the meridional tilts of PMSs within CIRs are influenced by small-scale structure of the parent coronal holes is further supported by the earlier results of *Broiles et al.* [2012]; they showed that the sign of meridional tilt changed for CIRs observed over several consecutive Carrington rotations. For the 3 CIRs studied in *Broiles et al.* [2013], no sign changes in  $\alpha$  were observed between ACE and Ulysses. This suggests two things: 1) CIR meridional tilt does not change drastically as CIRs move out in the heliosphere, and 2) the timescale for  $\alpha$  to change polarity is longer than the corotation time lag between ACE and Ulysses, (i.e., a few days). This conclusion could be tested more rigorously by comparing the meridional tilts of the same CIR at ACE and STEREO A and B, as the latter two spacecraft move away from the Earth, and will be the subject of a later study.

*Table 2: A summary of how theoretical predictions compare with observations. The table columns from left to right: CIR number, observing spacecraft, model, CIR azimuthal tilt, CIR meridional tilt, and predicted solar wind’s origin on the Sun. Predictions in agreement, disagreement, or not available are respectively marked with a checkmark, x, or N/A.*

#	Spacecraft	Model	$\epsilon$	$\alpha$	Origin
1	ACE	WSA-Enlil	✓	x	✓
		MAS-Enlil	✓	x	✓
	Ulysses	WSA-Enlil	✓	x	✓
		MAS-Enlil	✓	x	✓
2	ACE	WSA-Enlil	✓	✓	✓
		MAS-Enlil	✓	x	✓
	Ulysses	WSA-Enlil	x	x	✓
		MAS-Enlil	x	✓	✓
3	ACE	MAS-Enlil	x	✓	x
	Ulysses	MAS-Enlil	x	✓	x

## 4.2 Evolution of CIR Azimuthal Tilt

We observe a systematic change in  $\epsilon$  towards 0 for all three events. This qualitatively agrees with expectations and predictions of CIR evolution (not shown); i.e., the stream interface normal vector  $\hat{n}$ , asymptotically approaches  $\vec{R}$  as heliocentric distance increases. However, with the exception of CIR 1 the model results do not describe the behavior of the azimuthal tilt,  $\epsilon$ . The azimuthal tilt in CIR 1 behaves as expected from projections, but for CIR 2, the observed value of  $\epsilon$  did not rotate as much as projected at Ulysses. In CIR 3, the projection over-estimates  $\epsilon$  at Ulysses. We note that the simulation results of CIR azimuthal tilt are qualitatively similar to the analytical projections (not shown). Projections might be at odds with our observations because *Lee*’s model assumes that the solar wind is purely radial. Further, Enlil also assumes a radial solar wind in its initial conditions, regardless of WSA or MAS results. However in 74 events, *Broiles et al.* [2012] found that the azimuthal tilt,  $\epsilon$ , was not related to the expected Parker spiral at 1 AU. Since the

expected Parker spiral depends on local azimuthal flows [Forsyth *et al.*, 2001], we suggest that the discrepancy between the observed  $\epsilon$  and projected values could have occurred as a result of such transverse flows while the CIR was between the Sun and the Earth.

### 4.3 Conclusions

In conclusion, evolution of CIR meridional tilt was not well predicted by the models, which suggests that fine structure along the coronal hole boundary may be important for the local PMS orientation. Evolution of the azimuthal tilt was also not well predicted by the models, possibly because the models assume that the initial solar wind is purely radial.

*Acknowledgments:* The original paper was supported by the NASA grants NNX08AK87G, and NNX07AG85G and the NSF grant NSF-ATM 0962666. We thank the instrument teams and PIs, for SWEPAM (D.J. McComas), SWOOPS (D.J. McComas), MAG (C.W. Smith) and FGM (A. Balogh). Additionally, we recognize the CCMC, D. Odstrcil, C.N. Arge, Y.M. Wang, N.R. Sheeley, and R. Lionello, all of whom have made this work possible. Additionally, we thank the co-authors of the original paper.

## References

- Acuña *et al.* (1995), *Space Sci. Rev.*, 71, 5–21.
- Antiochos, S. K. *et al.* (2011), *Space Sci. Rev.*, doi:10.1007/s11214-011-9795-7.
- Arge, C. N., and V. J. Pizzo (2000), *JGR*, 105, 10,465–10,480, doi:10.1029/1999JA900262.
- Arge, C. N. *et al.* (2004), *JASTP*, 66, 1295–1309, doi:10.1016/j.jastp.2004.03.018.
- Balogh, A. *et al.* (1992), *A&AS*, 92, 221–236.
- Bame, S. J. *et al.* (1992), *A&AS*, 92, 237–265.
- Belcher, J. W., and L. Davis (1971), *JGR*, 76, 3534–3563.
- Broiles, T. W., M. I. Desai, and D. J. McComas (2012), *JGR*, 117, 21 PP., doi:10.1029/2011JA017288.
- Broiles, T. W., M. I. Desai, C. O. Lee, and P. J. MacNeice (2013), *JGR*, pp. n/a–n/a, doi:10.1002/jgra.50482.
- Clack, D., R. J. Forsyth, and M. W. Dunlop (2000), *GRL*, 27, 625.
- Crooker, N. U., E. M. Appleton, N. A. Schwadron, and M. J. Owens (2010), *JGR*, 115, 11,101.
- Forsyth, R. J., A. Balogh, and E. J. Smith (2001), *Space Sci. Rev.*, 97, 161–164.
- Fränz, M., and D. Harper (2002), *Planet. and Space Sci.*, 50(2), 217–233.
- Gosling, J. T. *et al.* (1993), *GRL*, 20, 2789–2792.
- Jian, L. K. *et al.* (2011), *Sol. Phys.*, 273, 179–203, doi:10.1007/s11207-011-9858-7.
- Khrabrov, A. V., and B. U. Ö. Sonnerup (1998), *JGR*, 103, 6641–6652.
- Lee, C. O. *et al.* (2009), *Sol. Phys.*, 254, 155–183.
- Lee, M. A. (2000), *JGR*, 105, 10,491–10,500.
- Lionello, R., J. A. Linker, and Z. Mikić (2003), in *SOLAR WIND 10*, vol. 679, pp. 222–225.
- McComas, D. J. *et al.* (1998), *Space Sci. Rev.*, 86, 563–612.
- Neugebauer, M., D. R. Clay, and J. T. Gosling (1993), *JGR*, 98, 9383–9389.
- Neugebauer, M., *et al.* (1998), *JGR*, 103, 14,587–14,600, doi:10.1029/98JA00798.
- Odstrcil, D. (2003), *Adv. in Space Res.*, 32, 497–506, doi:10.1016/S0273-1177(03)00332-6.
- Owens, M. J. *et al.* (2008), *Space Weather*, 6, 08,001, doi:10.1029/2007SW000380.
- Paschmann, G., and P. W. Daly (1998), ISBN 1608-280X
- Pizzo, V. J. (1991), *JGR*, 96, 5405–5420.
- Schwenn, R. (1990), in *Physics of the Inner Heliosphere I*, p. 99.
- Smith, C. W. *et al.* (1998), *Space Sci. Rev.*, 86, 613–632.
- Sonnerup, B. U. O., and L. J. Cahill (1967), *JGR*, 72, 171.
- Stone, E. C. *et al.* (1998), *Space Sci. Rev.*, 86, 1–22.
- Wang, Y.-M., and N. R. Sheeley (1990), *Ap.J.*, 355, 726–732, doi:10.1086/168805.
- Wenzel, K. P., R. G. Marsden, D. E. Page, and E. J. Smith (1992), *A&AS*, 92, 207.
- Zurbuchen, T., and I. Richardson (2006), *Space Sci. Rev.*, 123, 31–43.